Review

Not peer-reviewed version

Fatigue Crack Growth Models Applied to Additive Manufactured Electron Beam Melted Ti6Al4V: A Review

Nicole Atmadja and Mamidala Ramulu *

Posted Date: 23 March 2026

doi: 10.20944/preprints202603.1671.v1

Keywords: powder bed fusion; electron beam melting; additive manufacturing; Ti6Al4V; fatigue crack growth; damage tolerance

Review

Fatigue Crack Growth Models Applied to Additive Manufactured Electron Beam Melted Ti6Al4V: A Review

Nicole Atmadja and Mamidala Ramulu *

Department of Mechanical Engineering, University of Washington, Seattle, WA 98195, USA
* Correspondence: ramulum@uw.edu

Abstract

This article comprehensively reviews the fatigue crack growth (FCG) models applied to Ti6Al4V alloy manufactured by electron beam melting (EBM) powder bed fusion (PBF). The current progress in FCG analytical and numerical models and their application to EBM Ti6Al4V are reviewed. Many experimental data for the creation of historic FCG models were based on conventionally manufactured (CM) aluminum alloys and various steels. With the growth of additive manufacturing (AM), recent literature has applied traditional models and modified new models to EBM Ti6Al4V and validated their use as accurate predictive models for the da/dN-ΔK curve and ΔK_{th}.

Keywords: powder bed fusion; electron beam melting; additive manufacturing; Ti6Al4V; fatigue crack growth; damage tolerance

---

1. Introduction

With the rapid growth of metal additive manufacturing (AM), many industries have shown interest in incorporating it as a standard manufacturing method due to its benefits, including printing at near-net shape, building complex geometries, and reducing part count by combining multiple parts into one. These benefits of AM can result in significant cost and weight savings. Ti6Al4V is a titanium alloy that is known as the "workhorse" of the aerospace industry due to its high strength-to-weight ratio, corrosion resistance, and superior properties that balance strength and ductility. One of the most widely used AM processes is a powder bed fusion (PBF) process called electron beam melting (EBM).

One major hurdle to fully incorporating EBM Ti6Al4V into the aerospace industry is the uncertainty around its damage tolerance (DT) to fatigue cracks. Fatigue cracks tend to initiate from manufacturing/material discontinuities (grooves, scratches, burrs, tears, surface treatments, porosity, etc.) [1]. By predicting the rate of fatigue crack growth, DT design allows some amount of damage to a structure before repair/replacement is required. One of the reasons why fatigue cracks remain a major cause of structural failures in aircrafts [2] is because "short cracks" initiate from these defects and many FCG models are based on "long crack" testing standards (eg. ASTM E647 [3]). Short cracks are known to grow more quickly than long cracks [4–7], so the threshold stress intensity factor (SIF) range for long cracks (ΔK_{th}) may not be an applicable threshold for the realistic onset of crack growth.

With the advancement of analytical models and computational methods, an area of research interest has been to develop a model that can accurately predict FCG of AM parts specifically for DT analysis. Due to the history of FCG models and its relationship to the aerospace industry, many experimental data for the creation of traditional models were based on aluminum alloys and various steels, and may have been taken before more sophisticated crack growth measuring techniques were available [8]. With the growth of AM and the accumulation of FCG data, recent literature has used

doi:10.20944/preprints202603.1671.v1

traditional models and created new modified models and applied them to AM metals, including EBM Ti6Al4V [5,9–26].

2. Electron Beam Melting Process

The Arcam A2X EBM machine is a PBF process that begins by preheating a stainless-steel build plate placed at the center of the build chamber. Gravity feeds the Ti6Al4V powder down from the two powder hoppers on either side of the build chamber, where a rake slides across to spread and evenly distribute the powder onto the build plate. The electron beam selectively melts this layer of powder according to the build instructions from a CAD model. After the completion of one layer, the build platform lowers by one layer height (eg. 50µm), and the process is repeated layer-by-layer until the entire build is complete, shown in **Figure 1**. EBM manufacturing is commonly associated with producing titanium parts mostly due to its increased build chamber temperature of 750°C, which acts as an annealing step that allows parts to be built with negligible residual stresses that reduce part warping. The EBM chamber is maintained in a near-vacuum environment, reducing oxygen pick-up and contamination. However, due to the relatively large powder size of 45-105µm, EBM-produced parts have a higher surface roughness.

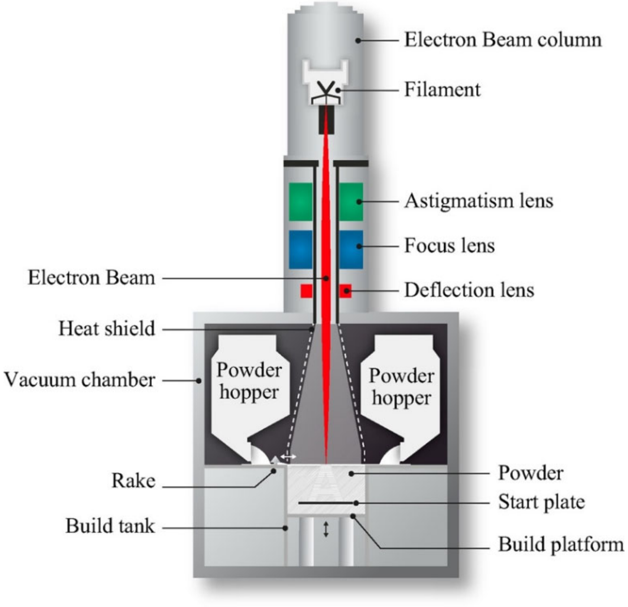

Figure 1. Schematic of the EBM build chamber [27,28].

3. FCG Models

With the introduction of fracture mechanics concepts in the 1950s, many FCG models were developed from linear-elastic fracture mechanics (LEFM) assumptions. Under LEFM, the plastic zone at the crack tip is considered small relative to the size of the specimen, so small-scale yielding (SSY) and bulk elastic behavior can be assumed. Because this is the simplest and most straightforward way to model FCG, much of the available data and models used in the literature use LEFM assumptions to predict crack growth and the determination of ΔK_{th} for long and short cracks.

3.1. da/dN-ΔK Curve

The log-log da/dN-ΔK curve is the most widely used illustration of FCG, which includes the near-threshold Region I, steady crack growth Region II, and overload Region III.

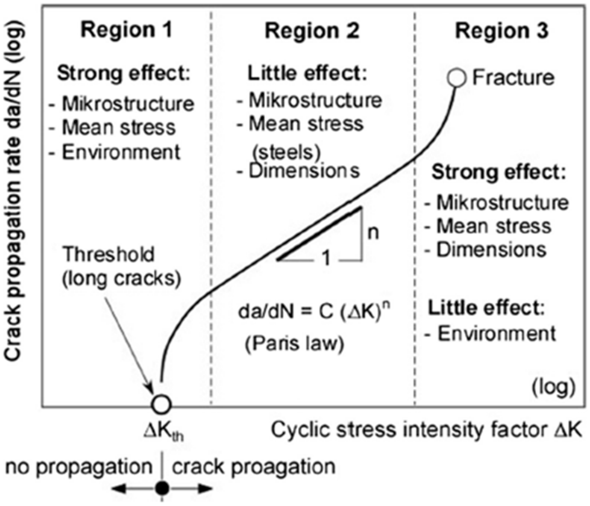

Figure 2. da/dN-ΔK FCG curve composed of Region I, II, and III [7].

This curve uses the SIF range (ΔK) as the crack driving force, which is derived from linear-elastic stress fields, and is defined as:

$$\Delta K = Y \Delta\sigma \sqrt{\pi a} \tag{1}$$

$$\Delta K = K_{max} - K_{min} \tag{2}$$

where Y is a constant geometry factor (Y=0.65 for surface cracks and Y=0.5 for internal cracks), Δσ is the applied load, and a is the crack length. The da/dN-ΔK curve was an important contribution because it implied that the crack growth rate is only dependent on ΔK (geometry, load, and the crack length). The simplicity of this curve influenced the development and evolution of many future analytical models with slight variations, many of them attempting to capture the non-continuum FCG behavior in Region I and short crack growth. A table summarizing each of the discussed FCG models is shown in **Table 1.** FCG models that predict the da/dN-ΔK curve and what region they apply to.**Table 1** including which region they apply to.

Proposed in 1963, Paris Law [29] is still extensively used for first order fatigue life predictions when limited data is available. It is commonly used because of its simplicity; it only requires 2 parameters (C and m) that are easy to obtain by curve-fitting with experimental data:

$$\frac{da}{dN} = C(\Delta K)^m \tag{3}$$

Paris Law uses a power law relationship to describe the steady crack growth behavior in Region II of the da/dN-ΔK curve on a log-log scale, where the 2 parameters C and m are empirically fit as the y-intercept and slope of the curve, respectively. Paris law is the foundation for many future adaptations of da/dN-ΔK FCG modeling, but although widely used and a good representation of Region II behavior, it neglects the near-threshold Region I and overload Region III. It also doesn't consider stress ratio (R) effects and there is no physical meaning behind the C and m constants, they are simply representative of the curve fitting technique used.

Table 1. FCG models that predict the da/dN-ΔK curve and what region they apply to.

Model	Equation	Region
1963: Paris Law [29]	$\frac{da}{dN} = C(\Delta K)^m$	II
1967: Forman [30]	$\frac{da}{dN} = \frac{C(\Delta K)^m}{(1-R)K_c - \Delta K}$	II-III

1970: Elber [31]	$\frac{da}{dN} = C(\Delta K_{eff})^m = C(U\Delta K)^m$	I
1970: Walker [32]	$\frac{da}{dN} = C\left[\frac{\Delta K}{(1-R)^{1-\gamma}}\right]^m$	III
1970: Hartman-Schijve [33]	$\frac{da}{dN} = \frac{C(\Delta K - \Delta K_{th})^m}{(1-R)K_c - \Delta K}$	I-III
1972: Klesnil & Lukas [34]	$\frac{da}{dN} = C(\Delta K^m - \Delta K_{th}^m)$	I
1990: NASGRO	$\frac{da}{dN} = C\left[\left(\frac{1-f}{1-R}\right)\Delta K\right]^m \frac{(1-\frac{\Delta K_{th}}{\Delta K})^p}{(1-\frac{K_{max}}{K_c})^q}$	I-III
2014: Hartman-Schijve Variant [35]	$\frac{da}{dN} = D\left(\frac{\Delta K - \Delta K_{thr}}{\sqrt{1 - K_{max}/A}}\right)^p$	I-III

In 1967, to address 2 of these limitations, Forman [30] adapted the Paris Law to include the overload Region III and consider stress ratio effects. The Paris Law was divided by a factor that approaches 0 as ΔK increases to a critical level K_c (fracture toughness):

$$\frac{da}{dN} = \frac{C(\Delta K)^m}{(1-R)K_c - \Delta K} \tag{4}$$

While Forman's contribution included Region III, in 1972, Klesnil and Lukas [34] introduced an equation to model ΔK_{th} in Region I. This equation was based on a power law formulation like Paris Law, but did not include Region II-III and only modeled Region I:

$$\frac{da}{dN} = C(\Delta K^m - \Delta K_{th}^m) \tag{5}$$

Focusing on Region I, Elber [31] introduced the concept of crack closure in 1970 stating that below a certain ”opening” SIF (K_{op}) where the crack faces are not in contact, there is no crack growth. Therefore, Elber introduced an effective SIF range ΔK_{eff} that can be substituted into Paris Eq. (3):

$$\Delta K_{eff} = K_{max} - K_{op} \tag{6}$$

$$\frac{da}{dN} = C(\Delta K_{eff})^m \tag{7}$$

Elber further proposed a crack closure ratio U:

$$U = \frac{\Delta K_{eff}}{\Delta K} \tag{8}$$

$$\frac{da}{dN} = C(U\Delta K)^m \tag{9}$$

The 3 types of crack closure effects include plasticity-, roughness-, and oxide-induced, and they have been used to explain the influence of stress ratio on FCG and the faster crack growth rates of short cracks that don't experience crack closure effects. Closure effects are mostly present in Region I, where ΔK_{th} decreases with increasing stress ratio [10,19,36]. It is also observed that closure effects are minimal at higher stress ratios above R=0.5 [37].

Based on FEA observations, Newman [38] defined a crack closure function f that is the effective stress ratio when crack closure effects are considered:

$$f = \frac{K_{op}}{K_{max}} \tag{10}$$

The most common method for obtaining K_{op} is the Adjusted Compliance Ratio (ACR) method that is included in the FCG standard testing procedure ASTM E647 [3].

In 1970, Walker [32] proposed a modification to the Paris Law by adding the influence of stress ratio. They defined a new ΔK that accounts for stress ratio and allows all ΔK data to result in the same line after curve-fitting for some empirical constant γ:

$$\frac{da}{dN} = C\left[\frac{\Delta K}{(1-R)^{1-\gamma}}\right]^m \tag{11}$$

The empirical constant γ is a material constant that indicates how strongly the stress ratio affects crack growth rate. For many traditional metals, γ=0.5, but can range from 0.3-1.0.

Although Walker's contribution considered stress ratio effects, this equation still only applied to Region II. And adding a third empirical parameter that requires data from many different stress ratios makes the equation more complicated. However, at this point, the crack growth rates of Region II and III were able to be predicted accurately with the models available.

To combine Regions I-III into a single model, in 1970, Hartman and Schijve [33] made empirical corrections to the Region I and Region III terms from Walker's Eq. (11). Observing that crack growth was slower in Region I, they suggested that da/dN should be related to how much ΔK exceeds the threshold value, so that $\Delta K - \Delta K_{th}$ is in the numerator. Similarly observing that crack growth was faster in Region III, they included in the denominator the rapid acceleration as K_{max} approaches K_c. They further replaced K_c with the max cyclic fracture toughness (A). ($A=K_{max,c}=K_{min,c}/\Delta K_c$). The modified equation becomes:

$$\frac{da}{dN} = D\left[\frac{\Delta K - \Delta K_{th}}{(1 - K_{max}/A)^q}\right]^p \tag{12}$$

where D and p respectively, become the y-intercept and slope curve-fitting parameters that are found by relating da/dN with this new modified crack driving force. This equation produces a sigmoid shape, where the curve steepens at both low and high ends and includes Regions I-III on the da/dN-ΔK curve. The drawback of this model is that ΔK_{th} is sensitive to stress ratio, and that the value of ΔK_{th} must already be known.

The Hartman-Schijve equation was later simplified by using Schwalbe's [39] crack driving force, where the constant q=1/2. Further, Jones [35] altered the threshold value as an "apparent threshold SIF range" (ΔK_{thr}) that can be applied to both short and long crack threshold values:

$$\Delta\kappa = \frac{\Delta K - \Delta K_{thr}}{\sqrt{1 - \frac{K_{max}}{A}}} \tag{13}$$

This gives a modified Hartman-Schijve variant equation using the Schwalbe factor:

$$\frac{da}{dN} = D(\Delta\kappa)^p \tag{14}$$

The NASGRO equation is used in several FCG computer programs (NASGRO, AFGROW, FASTRAN) and is widely used in the aerospace industry to compute the operational life of a component. Developed by NASA in the 1990s, the NASGRO equation was based on a combination of the above mentioned equations to model Regions I-III:

$$\frac{da}{dN} = C\left(\frac{1-f}{1-R}\right)^m \Delta K^{(m-r)} \frac{(\Delta K - \Delta K_{th})^r}{\left(1 - \frac{K_{max}}{A}\right)^q} \tag{15}$$

where r and q are curve-fitting constants (r controls the lower Region I part of the curve and q controls the upper Region III part of the curve). And f is the Newman crack closure function from Eq. (9) (when crack closure is not present, f=R and the (1−f)/(1−R) term cancels out).

The Hartman-Schijve variant Eq. (14) and the NASGRO Eq. (15) both model FCG in Regions I-III. In addition to analytical models, numerical simulations have also been used to predict FCG.

3.2. Numerical Simulations

Numerical simulations have obvious advantages for FCG prediction due to the time frame of experimental fatigue testing, especially in the near-threshold Region I. Finite element methods (FEM) are popularly used to predict FCG, time to failure, and crack interaction with its microstructure.

In 1981, Newman [38] used FEA to observe plasticity-induced crack closure and proposed the strip-yield model to reproduce results more computationally efficiently. The strip yield model predicts plasticity-induced crack closure and ΔK_{eff} in FCG and is the basis for NASGRO's closure model. The model uses bars of a rigid plastic material surrounding the crack, illustrated in **Figure 3**. Region 1 is elastic continuum, Region 2 is modeled with the perfectly plastic material mimicking the plastic zone, and Region 3 is in the wake of the crack, which uses the same plastic material, but the elements are split and can only transfer compressive (not tensile) loads.

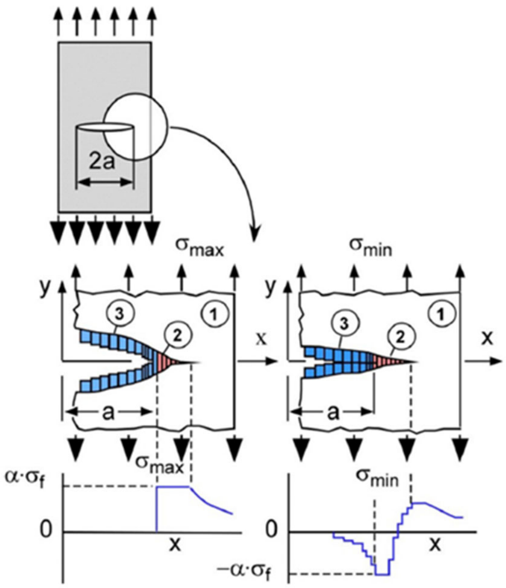

Figure 3. Schematic of the strip-yield model [9].

An extension to traditional FEM is the extended FEM (XFEM) proposed in 1999 [40]. XFEM takes advantage of the partition of unity property of finite elements that allow enrichment functions to be added to the finite element shape function that approximates the behavior between 2 nodes. The enrichment function allows a specific approximation in a region of interest.

Another recent numerical simulation popular in the literature is peridynamics (PD), developed by Silling in 2000 [41]. Contrary to traditional continuum mechanics that use partial differential equations, PD uses integral equations, meaning that they don't require spatial derivatives and are able to handle discontinuities like damage, fracture, and crack growth. PD was developed in 2000 as a "bond-based" model that assumed that forces between 2 bonds are pairwise and symmetric and that the material response is linear elastic and isotropic.

In 2010, PD was extended to a "state-based" model that was able to evaluate multiple bonds collectively within a neighborhood, and material response could be anisotropic and plastic [42]. By 2014, PD was applied to FCG, as it was particularly useful for modeling discontinuities like crack growth [43]. The PD equation is a reformulation of Newton's law F=ma, where the right-hand side are the forces and the left-hand side are the mass and acceleration terms:

$$\rho(x)\ddot{u}(x,t) = \int_{H_x} f(u(x',t) - u(x,t), x' - x)\, dV_{x'} + b(x,t) \qquad (16)$$

where x is the position of a point, x′ is the position of a neighboring point, ρ(x) is the mass density at point x, $\ddot{u}$(x,t) is the acceleration of the material at point x and time t, H_x is the "horizon" (ie. all nearby points x′ within a certain radius), u(x′,t)−u(x,t) gives the relative displacement between x′ and x, x′−x is the relative position between x′ and x, and b(x,t) are external body forces. The function defines the force between 2 points depending on their relative displacement and position and integrates over the horizon for the entire neighborhood of points. Instead of observing the interaction between only 2 points, PD integrates all the points within a horizon [43]. Ultimately, based on Paris Law, the PD relation is:

$$\frac{da}{dN} = \lambda B \varepsilon_{core}^{m} \tag{17}$$

where A is a positive parameter and ε_{core} is the bond strain, referring to the bond at the crack tip on the verge of breaking. m is the same value as the Paris exponent from Eq. (3).

In addition to predicting FCG, the ΔK_{th} value in Region I is the threshold below which long cracks do not propagate. However, as mentioned earlier, short cracks grow at a faster rate than long cracks, meaning that short cracks may propagate below this threshold. Many models have focused on predicting ΔK_{th} for long and short cracks.

3.3. Predicting ΔK_{th}

With standard long crack FCG testing procedures, the determination of ΔK_{th} requires many specimen to account for variability, it is expensive, and time consuming. Further, the ASTM E647 standard simply defines ΔK_{th} as the ΔK value when da/dN is extrapolated to approximately 10^{-10}m/cycle on the log-log da/dN-ΔK curve using a K-decreasing test method. This method also does not consider short crack growth below the ΔK_{th} value. Due to these reasons, many models have been developed that are analytically- or empirically-based to approximate ΔK_{th} for long and short cracks.

Short cracks can be categorized as "microstructurally small"/"microcrack" or "physically small". **Table 2** below defines approximate size ranges of short and long cracks.

Table 2. Approximate size range for short and long cracks.

Crack Type	Length	Region
Microstructurally short cracks	<grain size (<10µm)	Before Region I
Physically short cracks	~a few grains (10-500µm)	Transition to Region I
Long cracks	>>grain size (>1mm)	Region I-III

Table 3 below summarizes each of the discussed ΔK_{th} models and indicates which type of crack size they apply to.

Table 3. Models that predict ΔK_{th} and what crack size they apply to.

Model	Equation	Crack Size
1979: El-Haddad Approach [44]	$\Delta K_{th,SC} = Y\Delta\sigma_e\sqrt{\pi a_o}$	Short
2002: Murakami $\sqrt{area}$ Parameter [45]	$\Delta K_{th,SC} = Y\Delta\sigma_e\sqrt{\pi\sqrt{area_o}}$	Short
1997: Stress Ratio Curve [37]	$\Delta K_{th} = (K_{max,o} + \beta_o R)(1 - R)$ when $R < 0.5$ $\Delta K_{th} = \frac{1-R}{1-R-\alpha_o}\Delta K_o$ when $R > 0.5$	Long
2018: HV Relation [21,22]	$\Delta K_{th} = 3.3 \times 10^{-3}(HV + 120)(\sqrt{area})^{1/3}$	Long
2020: Bi-Parametric Model [23]	$\Delta K_{th} = \alpha \cdot \ell^{\beta} + \zeta \cdot HV^{\delta}$	Long

In order to satisfy DT requirements, it is necessary to predict short crack growth that can initiate from manufacturing/material flaws. The slip mechanism for fatigue crack initiation and FCG are the same. This allows the fatigue limit of "defect-free" specimen ($\Delta\sigma_e$) from S-N data to be related to the threshold value (ΔK_{th}) from FCG data. When $\Delta\sigma_e$ and ΔK_{th} are known, they can be related by the Kitagawa-Takahashi diagram (KT diagram) [46] that plots the fatigue strength ($\Delta\sigma_{th}$) against the crack length (a) on a log-log scale. This relationship provides either the fatigue strength of a specimen when a defect is present or the max allowable crack size for a given applied load. **Figure 4** shows a KT diagram with 3 zones that are associated with microcracks (Zone 1), physically short cracks (Zone 2), and long cracks (Zone 3). This plot shows that fatigue strength diminishes as the crack length increases. (d_1 is the length of the microcrack threshold and d_2 is the length of the long crack threshold).

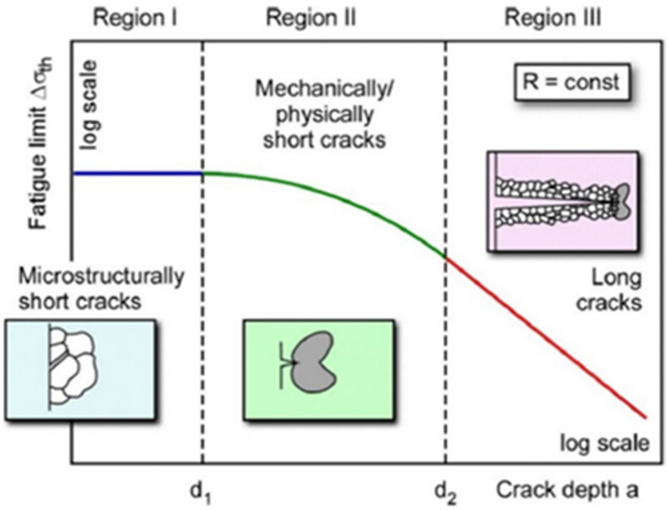

Figure 4. Kitagawa-Takahashi (KT) diagram [9].

In this diagram, Zone 1 and Zone 3 are easily known, where Zone 1 can be approximated as the defect-free fatigue limit:

$$\Delta\sigma_{th} = \Delta\sigma_e \tag{18}$$

$\Delta\sigma_e$ is plot as a horizontal line in Zone 1. Zone 3 is estimated by the threshold SIF range from Eq. (2):

$$\Delta\sigma_{th} = \frac{\Delta K_{th}}{\sqrt{\pi a}} \tag{19}$$

ΔK_{th} is plot with a slope of −1/2 in Zone 3 due to its exponent from the square root in the denominator. Both of these lines from Eq. (18) and Eq. (19) intersect at a point a_o. Introduced in 1979, the El-Haddad [44] parameter a_o describes the theoretical defect size that does not affect fatigue strength:

$$a_o = \frac{1}{\pi}\left(\frac{\Delta K_{th}}{\Delta\sigma_e}\right)^2 \tag{20}$$

However, realistically, the behavior around this point is not linear. There are 3 popular methods for approximating this nonlinear behavior in Zone 2: El-Haddad's approach [44,47], the cyclic R-curve method [17,36], and using Murakami's $\sqrt{area}$ parameter [45].

Based on the KT diagram, El-Haddad defined a fictitious crack length $a+a_o$ to express a continuous curve. Since Zone 2 applies to short cracks, $\Delta K_{th,SC}$ is used, so Eq. (19) is modified as:

$$\Delta\sigma_{th} = \frac{\Delta K_{th,SC}}{\sqrt{\pi(a+a_o)}} \tag{21}$$

Rearranging Eq. (20), $\Delta K_{th,SC}$ is substituted into Eq. (21) to approximate $\Delta\sigma_{th}$ as a function of $\Delta\sigma_e$, a, and a_o:

$$\Delta\sigma_{th} = \Delta\sigma_e\sqrt{\frac{a_o}{a + a_o}} \tag{22}$$

Similarly, ΔKth,SC is found as:

$$\Delta K_{th,SC} = \Delta K_{th}\sqrt{\frac{a}{a + a_o}} \tag{23}$$

In 1988, Tanaka and Akiniwa [36,48] introduced the cyclic Resistance Curve (R-Curve). While the KT diagram relates short and long crack fatigue limit $\Delta\sigma_{th}$ and uses crack length a, the R-Curve relates short and long crack ΔK_{th} and uses crack extension Δa. The R-curve method is obtained experimentally by incrementally increasing the applied load until the crack arrests at each load step. This allows multiple data points from a single specimen and leads to a curve shown in **Figure 5** [17], where the data approaches a ΔK_{th} value as crack extension (Δa) increases. This curve assumes crack closure buildup as the main mechanism for FCG resistance. In this context, a material has an intrinsic threshold $\Delta K_{th,eff}$ that is material-dependent, and an extrinsic threshold $\Delta K_{th,op}$ that is affected by factors such as microstructure, stress ratio, and environment. Given an applied load, a crack of a certain length will arrest (below the R-curve) or propagate (above the R-curve).

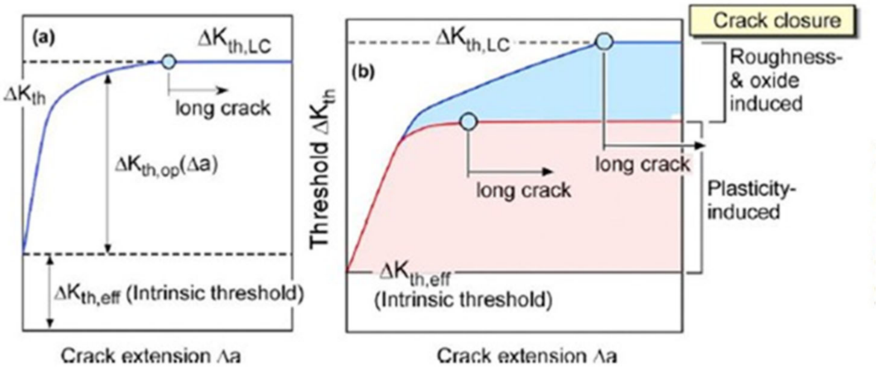

Figure 5. Cyclic R-curve and the contributions from different crack closure effects [17].

The information presented by the R-curve is synonymous with that of the KT diagram; it is possible to plot the KT diagram from the R-curve and vice versa since they both provide information about crack arrest loads.

In 2002, Murakami [45] determined that the fatigue limit $\Delta\sigma_{th}$ is the same as the threshold stress where small cracks do not propagate $\Delta K_{th,SC}$. Therefore, Murakami's $\sqrt{area}$ parameter [49] can be applied to the SIF range Eq. (1) by replacing the crack length a with the $\sqrt{area}$ and replacing ΔK applied to short cracks and Δσ with the fatigue limit:

$$\Delta K_{th,SC} = Y\Delta\sigma_{th}\sqrt{\pi\sqrt{area}} \tag{24}$$

Eq. (24) can be rearranged to solve for the initial defect size:

$$\sqrt{area_o} = \frac{1}{\pi}\left(\frac{\Delta K_{th,SC}}{Y\Delta\sigma_{th}}\right)^2 \tag{25}$$

Substituting and rearranging Eqs. (24) and (25) solves for $\Delta K_{th,SC}$ in terms of $\sqrt{area}$:

doi:10.20944/preprints202603.1671.v1

$$\Delta K_{th,SC} = \Delta K_{th}\sqrt{\frac{\sqrt{area}}{\sqrt{area}+\sqrt{area_o}}} \tag{26}$$

From testing on 16 different materials (various steels, aluminum, and brass that were annealed, quenched, or tempered) at R=-1 with different-sized small artificial defects, a positive linear relationship between $\Delta K_{th,SC}$ and $\sqrt{area}$ on a log-log scale, with a slope of 1/3 was found for all 16 materials [45], leading to a proportional relationship between the 2 variables:

$$\Delta K_{th,SC} \propto \left(\sqrt{area}\right)^{\frac{1}{3}} \tag{27}$$

Because the use of $\sqrt{area}$ implies short cracks/small defects, the relationship above only applies to $\sqrt{area}$<1000µm. Additionally, it was concluded that materials with higher Vickers hardness HV had higher $\Delta K_{th,SC}$ values. Using a least squares regression method on the 16 different materials, constants were found so that:

$$\Delta K_{th,SC} = 3.3\times10^{-3}(HV+120)\left(\sqrt{area}\right)^{\frac{1}{3}} \tag{28}$$

Where $\Delta K_{th,SC}$ is in MPa√m, HV is in kgf/mm^2, and $\sqrt{area}$ is in µm. Similarly, for the fatigue strength based on 2 types of carbon steel, on a log-log scale, there was a negative linear relationship between σ_{th} and $\sqrt{area}$ with a slope of −1/6, forming the relationship:

$$\sigma_{th} \propto \left(\sqrt{area}\right)^{-\frac{1}{6}} \tag{29}$$

Similarly using a least squares regression method to solve for constants gives the relationship:

$$\sigma_{th} = \frac{1.43(HV+120)}{\left(\sqrt{area}\right)^{\frac{1}{6}}} \tag{30}$$

Eq. (28) and Eq. (30) are only valid for HV≤400 because the experimental data showed a drastic drop in fatigue limit due to the presence of small defects and larger scatter in the data around HV>400 [45]. Another empirical formula developed for HV<400 is only in terms of HV and gives the ideal ("defect-free") upper bound fatigue limit:

$$\sigma_e = 1.6HV \pm 0.1HV \tag{31}$$

Building on Murakami's $\sqrt{area}$ parameter method, Rigon and Meneghetti [23] use a $\sqrt{area}$ approach to solve for the transition defect sizes on the KT diagram (**Figure 6**). They define a critical $\sqrt{area_c}$ between Zone 1 and 2 and a transition $\sqrt{area_t}$ between Zone 2 and 3. $\sqrt{area_c}$ is found by replacing the fatigue limit in Eq. (30) with the defect-free fatigue limit in Eq. (31):

$$\sqrt{area_c} = \left(\frac{1.43(HV+120)}{1.6HV}\right)^6 \tag{32}$$

$\sqrt{area_c}$ is the max defect size before it becomes damaging. $\sqrt{area_t}$ is found by replacing $\Delta K_{th,SC}$ in Eq. (28) with the long crack threshold ΔK_{th} to find the transition defect size between a short and long crack:

$$\sqrt{area_t} = \left(\frac{\Delta K_{th}}{3.3\times10^{-3}(HV+120)}\right)^3 \tag{33}$$

These values $\sqrt{area_c}$ and $\sqrt{area_t}$ are used to define the transition defect size, shown in **Figure 6**.

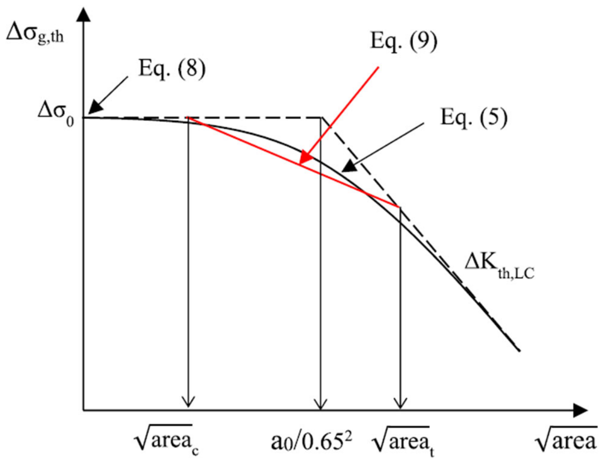

Figure 6. KT diagram showing critical $\sqrt{area_c}$ and transition $\sqrt{area_t}$ defect sizes [23].

In 1997, Doker [37] proposed a method for threshold determination by plotting ΔK_{th} against the stress ratio R that uses 4 independent curve-fitting parameters ($K_{max,o}$, ΔK_o, α_o, β_o) obtained from the linear portion of experimental data of CM steels and aluminum alloys plotted on $K_{max,th}$-R and ΔK_{th}-K_{max} curves. $K_{max,th}$ and ΔK_{th} values were obtained from K-decreasing tests following ASTM E647. Solving for ΔK_{th} of these linear regression lines gives 2 equations:

$$\Delta K_{th} = \left(K_{max,o} + \beta_o R\right)(1 - R)\ when\ R < 0.5 \tag{34}$$

$$\Delta K_{th} = \frac{1 - R}{1 - R - \alpha_o} \Delta K_o\ when\ R > 0.5 \tag{35}$$

These 2 equations are plot in **Figure 7** for a generic curve that takes into account the observations that ΔK_{th} decreases with increasing R until a critical R_c value ($R_c \approx 0.5$-0.6), where R becomes less influential [10,37].

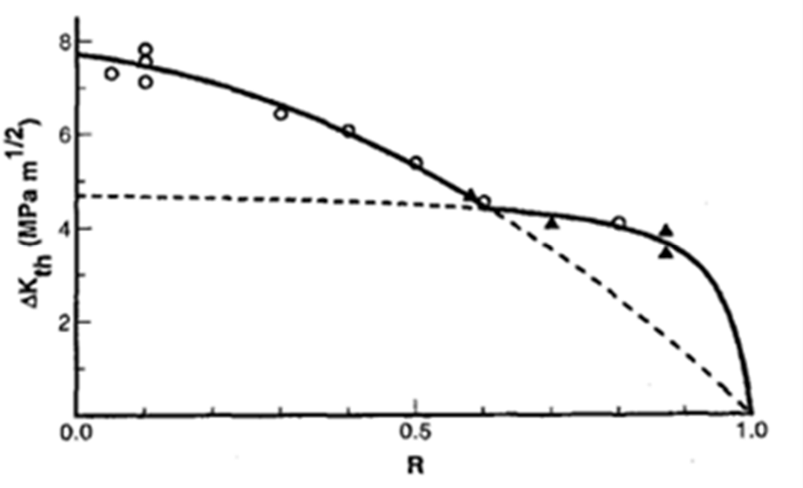

Figure 7. Doker's stress ratio curve [37].

In 1982, showing microstructural influence, Yoder [50] proposed a cyclic plastic zone-based model to predict ΔK_{th} based on YS and "effective grain size" (ℓ), For α/β titanium alloys like Ti6Al4V, ℓ is the α-lath thickness [51]. Instead of using the ASTM E647 definition of ΔK_{th}, Yoder described it as the "knee" on the da/dN-ΔK curve at the Region I-II transition and physically described it as the point when the size of the plastic zone at the crack tip equals the size of the effective grain size ($r_y^c \sim \ell$). The plane strain cyclic plastic zone size can be approximated as:

$$r_y^c = \frac{1}{8\pi}\left(\frac{\Delta K}{\sigma_{ys}}\right)^2 \tag{36}$$

Similarly showing microstructural influence, in 2020, [23] proposed a model that directly incorporates microstructural influence and Vicker's hardness on predicting ΔK_{th}. For Ti6Al4V, the influential microstructural feature is the α-lath thickness. On a log-log scale, [23] showed a negative linear relationship between ΔK_{th} and HV and a positive linear relationship between ΔK_{th} and α-lath thickness that led to the proposed equation:

$$\Delta K_{th} = \alpha \cdot \ell^{\beta} + \zeta \cdot HV^{\delta} \tag{37}$$

where α, β, ζ, and δ are coefficients that depend on R and are fit to the data, ℓ is the influential microstructural feature (α-lath thickness in μm for Ti6Al4V), and HV is in kgf/mm^2. Some drawbacks of this model are that it requires FCG data taken at multiple different stress ratios, there are 4 curve-fitting parameters, and there was a relatively large error ±20% with the experimental data. However, it gives a rationale for the material and microstructural influence.

4. FCG Models Applied to EBM Ti6Al4V

4.1. da/dN-ΔK Curve

Some of the above models were originally developed with CM aluminum or steel materials, but have recently been applied to AM EBM Ti6Al4V, verifying its potential to be used on this new material to predict FCG behavior and short and long crack ΔK_{th}.

Crack closure effects apply to EBM Ti64 [47], showing the same expected relationships as for CM materials: ΔK_{th} decreases with increasing stress ratio, with minimal closure effects at higher stress ratios above R=0.5. These relationships were true for both horizontal and vertical orientations and between AB and HT cases.

Using the Hartman-Schijve variant Eq. (14), when applied to AM Ti6Al4V, [14] found the D and p values to be: D=2.79×10^{-10} and p=2.12, obtained from curve-fitting with experimental data. Despite the AM process used (EBM, SLM, DMLS, LENS), different build orientations (horizontal, vertical), or post-processing applied (AB, HIP), the curves fell on the same master curve with variation coming only from ΔK_{thr} and A. This was also true for 77 other tests on various metals [5,15,16,52,53], implying that the parameters ΔK_{thr}, A, D, and p somehow account for all other factors, including microstructural influences. Using this equation, the contribution of microstructure is unclear [6], although it has been shown through other literature that microstructure is influential on material properties in general and in the near-threshold region for FCG.

The use of an apparent threshold SIF range ΔK_{thr} allows the flexibility for estimating short or long crack thresholds. Short crack prediction of $\Delta K_{th,SC}$ can be made by setting ΔK_{thr} to an arbitrarily small value (eg. ΔK_{th}=0.1MPa√m) [14]. For long crack prediction of ΔK_{th}, the use of the Hartman-Schijve variant predicts FCG in Regions I-III and can match empirical data by only adjusting 2 parameters: ΔK_{thr} and A, given curve-fitting parameters D and p that are constant for each material. **Figure 8** shows experimental data for various stress ratios, orientations, and post-process conditions taken from the literature [10,54–59].

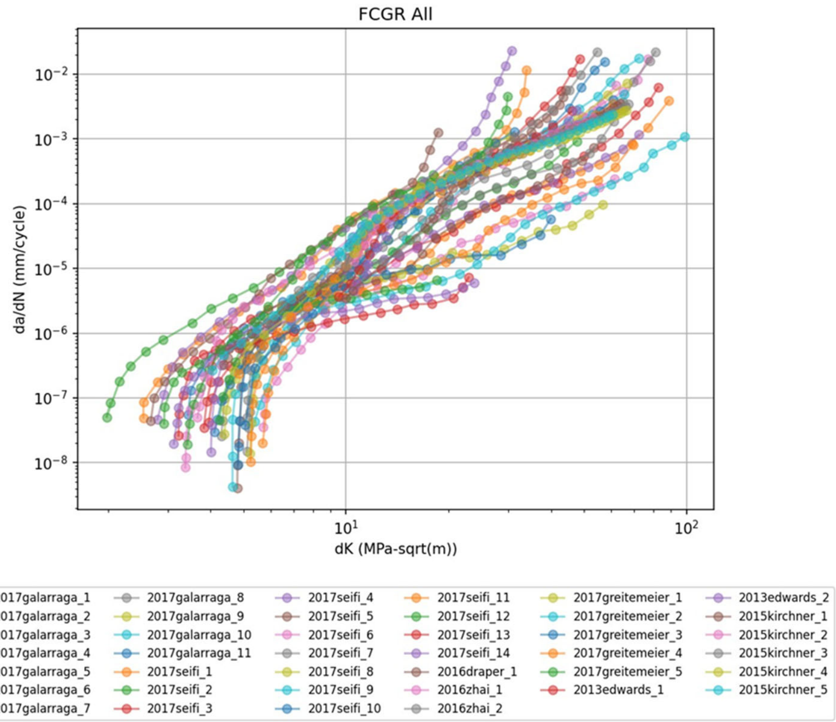

Figure 8. FCG experimental data of EBM Ti6Al4V for a variety of stress ratios, orientations, and post-process conditions [10,54–59].

Using data from the literature, **Figure 9** uses the Hartman-Schijve variant Eq. (14) to approximate FCG curves by stress ratio, orientation, and post-processing conditions.

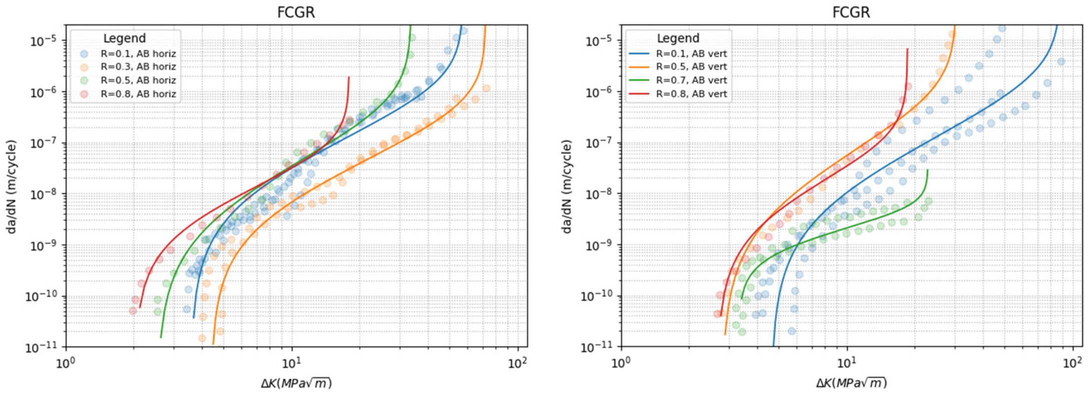

(**a**) (**b**)

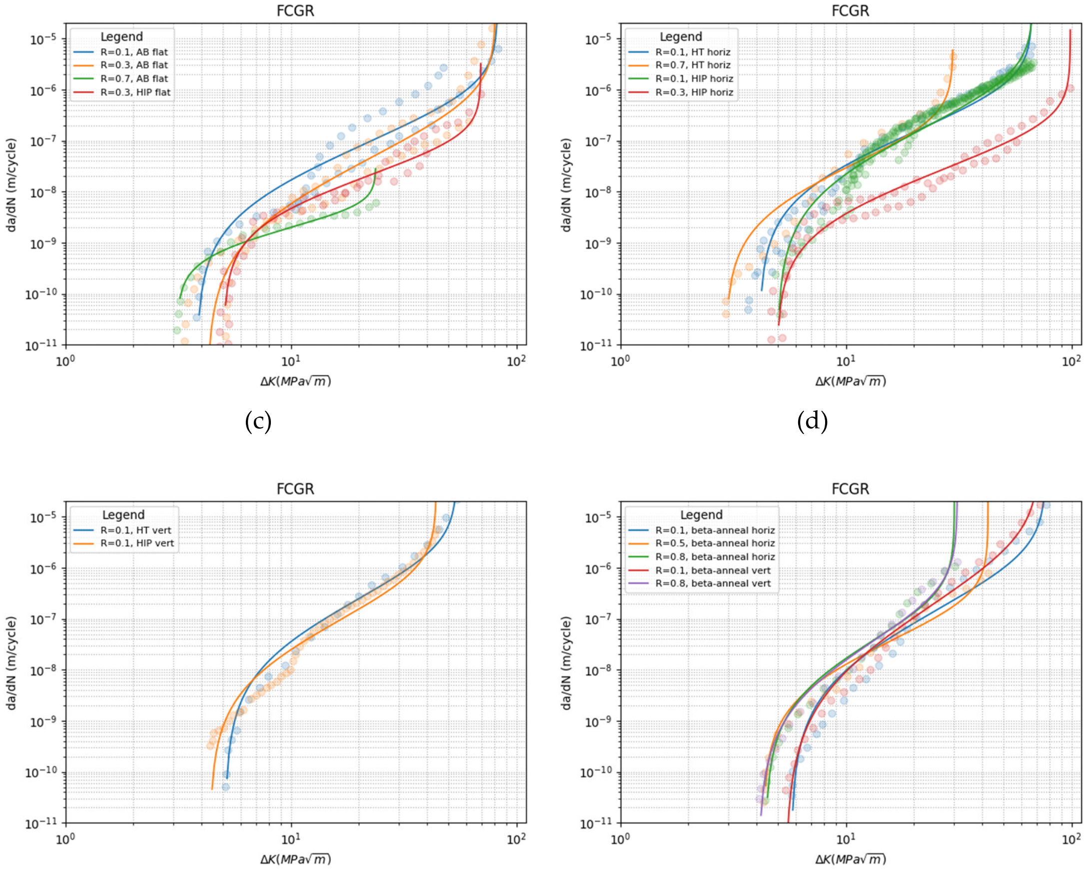

(c) (d)

(e) (f)

Figure 9. Hartman-Schijve variant equation applied to experimental data at different stress ratios, orientations, and post-processes [10,54–59].

4.2. Numerical Simulations

Some researchers have applied PD to FCG of AM titanium alloys [19,20]. [19] applied PD to a general AM Ti6Al4V material by simulating both equiaxed and columnar grains. They simulated coarser grains have greater FCG resistance than finer grains and modeled the deflection angle of cracks as they interact with α-laths at different angles. They showed more deflection when α-laths were perpendicular to the crack growth and less resistance when the α-laths were parallel along the crack growth direction. [20] used PD to simulate intergranular and transgranular crack growth depending on the size of the grains, as seen in **Figure 10** and validated with a vs. N curves from literature data in Region II of the FCG curve.

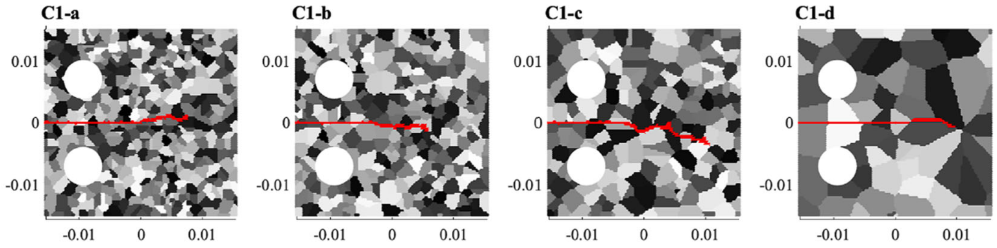

Figure 10. PD simulation showing crack growth for different sized equiaxed grains [20].

In 2024, [60] proposed a Whole Rate Region model that amends the PD equation to include Regions I-III and simulated FCG curves that aligned with experimental data. More recently, [61] proposed a multiscale model that uses tensile properties and microstructural information to create an FCG model that predicts the S-N curve of AM Ti6Al4V.

4.3. Predicting ΔK_{th}

Galarraga [10] applied Doker's stress ratio curve [37] to relate ΔKth with the stress ratio based on experimental data on EBM Ti6Al4V. They obtained a similar relationship between ΔK_{th} and stress ratio, with a critical R_c=0.5 for both AB and β-annealed specimen in both the horizontal and vertical orientations. They plotted a curve shown in **Figure 11** that follows the same trend as Doker's [37].

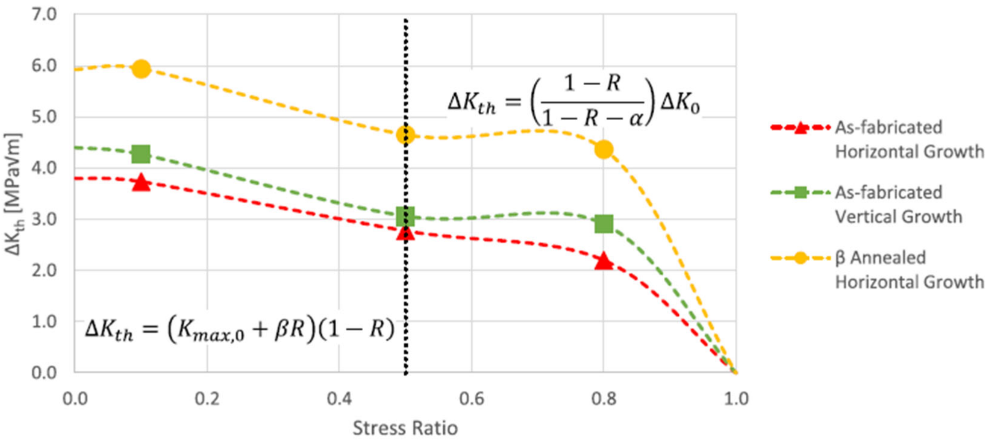

Figure 11. Stress ratio curve applied to EBM Ti6Al4V [10].

Based on 16 different materials, [21,22] applied Eq. (31) to EBM Ti6Al4V to obtain an approximate ideal upper bound σ_e=544-605MPa. Experimental data shows a fatigue strength of ~500-600MPa for the HIP+machined specimen; otherwise, the fatigue limit is much lower than predicted due to the inferior fatigue performance of AM compared to CM (due to high surface roughness and internal defects). This exemplifies the validity of Eq. (31) for EBM Ti6Al4V after HIP+machined post-processing.

As seen in **Figure 12**, [21] applied Murakami's relationship Eq. (28) to HIP+machined EBM Ti6Al4V at R=-1 and found the same constants and slope of 1/3 between ΔK_{th} and $\sqrt{area}$ on a log-log scale, showing application of Eq. (28) on EBM Ti6Al4V. However, they acknowledged that this relationship is too conservative for long crack ΔK_{th} estimation.

Authors have applied the KT diagram to EBM Ti6Al4V [17,21–24,26,62–64] using ElHaddad's approximation and Murakami's method. From these studies, they concluded that these approaches are applicable for approximations of EBM Ti6Al4V. [26] applied the KT diagram for heat treated AM Ti6Al4V, including EBM, shown in **Figure 13**.

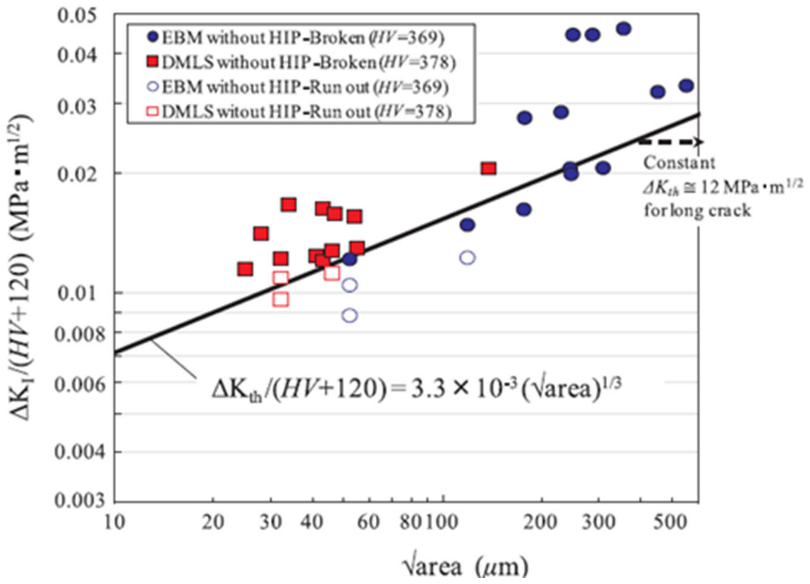

Figure 12. Predicting ΔKth based on HV from AM metals [21].

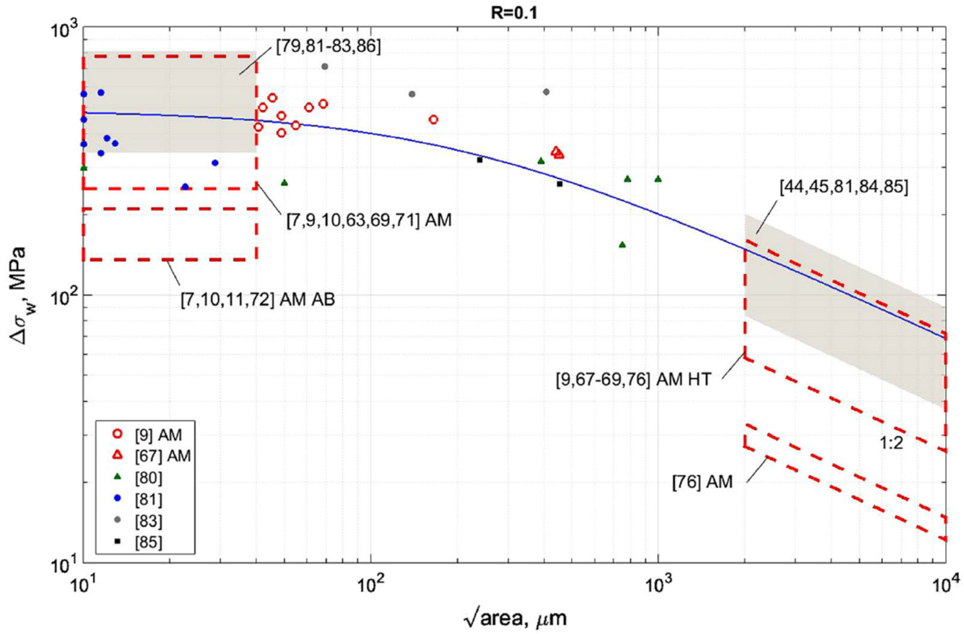

Figure 13. KT diagram applied to AM Ti6Al4V [26].

However, these authors only applied KT diagram to specimen that have been machined. It was acknowledged that this method is inaccurate for AB specimen due to the detrimental effects of surface roughness on fatigue strength. [22,64] recommended treating surface roughness as a long crack growth problem. [26] proposed a conversion factor to account for surface roughness effects by measuring $\sqrt{area}$ of subsurface pores at a depth of t=200μm:

$$\sqrt{area} = t \cdot \sqrt{10} \tag{38}$$

Additionally, [22,45] proposed an evaluation method for equivalent defect size $\sqrt{area_R}$:

$$\frac{\sqrt{area_R}}{2b} = 2.97\left(\frac{a}{2b}\right) - 3.51\left(\frac{a}{2b}\right)^2 - 9.74\left(\frac{a}{2b}\right)^3 \quad for \ \frac{a}{2b} \le 0.195 \tag{39}$$

$$\frac{\sqrt{area_R}}{2b} \approx 0.38 \; for \; \frac{a}{2b} \geq 0.195 \tag{40}$$

where the max value of max height S_a is used for a and the mean width of profile R_{sm} is used for 2b.

Other researchers [63] used the KT diagram to relate d_1, a_o, and d_2 values to microstructural features showing the dependence of microstructure in the short crack regime. They found that $a_o \sim 10\ell$, however the experimental data was based on CM steels, coppers, and aluminums at R= -1[13,23] used the Bi-Parametric model Eq. (37) and used alpha-lath thickness as the microstructural feature to estimate ΔK_{th}=6.82 MPa√m for EBM Ti6Al4V in the AB horizontal condition with a ±10% error with experimental data.

5. Conclusions

In this review article, the current state of the literature on FCG models on EBM Ti6Al4V was comprehensively discussed, reviewing both analytical and numerical models for predicting the da/dN-ΔK curve and ΔK_{th} in Region I, and simulating FCG behavior.

The literature has shown that the use of many analytical and numerical models is promising for the application of FCG of EBM Ti6Al4V. Many experiments have been done to validate their use. However, more experimental data is needed to account for the many variables that exist with AM, including stress ratio effects, specimen orientation, post-processing, build height, etc. In light of these promising developments, there is still a need for synergy between experimental characterizations, numerical simulations, and physical validation through the material microstructure.

With an understanding of the microstructure-property relationship, the material can be tailored to produce desired properties. While literature has mostly focused on α-lath thickness, there is a need for a complete microstructure characterization including other α and β features and their relationship to FCG in electron beam processed titanium alloy.

Author Contributions: Conceptualization, methodology, software, validation, formal analysis, investigation, resources, data curation, writing—review and editing, M.R. and N.A.; writing—original draft preparation, visualization, N.A.; supervision, project administration, funding acquisition, M.R. All authors have read and agreed to the published version of the manuscript.

Funding: This research was supported by Boeing-Pennell Professorship Funding (awarded to M. Ramulu by the Boeing Company). The authors would like to thank the department of Mechanical Engineering at UW-Seattle for the support provided during this study.

Data Availability Statement: No new data were created or analyzed in this study. Data sharing is not applicable to this article.

Acknowledgments: During the preparation of this manuscript/study, the authors used WebPlotDigitizer v5 for the purposes of extracting data from the literature. The authors have reviewed and edited the output and take full responsibility for the content of this publication.

Conflicts of Interest: The authors declare that this study received funding from the Boeing Company. The funder was not involved in the study design, collection, analysis, interpretation of data, the writing of this article or the decision to submit it for publication.

Abbreviations

The following abbreviations are used in this manuscript:

AB	As-built
ACR	Adjusted compliance ratio
AM	Additive manufacturing
CAD	Computer aided design
CM	Conventional manufacturing

CTOD	Crack tip opening displacement
DMLS	Direct metal laser sintering
DT	Damage tolerant
EBM	Electron beam melting
FCG	Fatigue crack growth
FEA	Finite element analysis
FEM	Finite element method
HIP	Hot isostatic pressing
HT	Heat treated
KT	Kitagawa-Takahashi
LEFM	Linear elastic fracture mechanics
LENS	Laser-engineered net shaping
NDT	Non-destructive testing
PBF	Powder bed fusion
PD	Peridynamics
R-Curve	Resistance curve
SIF	Stress intensity factor
SLM	Selective laser melting
SSY	Small-scale yielding
Ti6Al4V	Titanium 6-Aluminum 4-Vanadium alloy
XFEM	Extended finite element method

Nomenclature

The following nomenclature are used in this manuscript:

A	Apparent cyclic fracture toughness
a	Crack length
a_o	El-Haddad's parameter in Eq. (20)
$\sqrt{area}$	Murakami's defect size estimation
$\sqrt{area_c}$	Critical and transition defect size estimation in Eq. (32)
$\sqrt{area_t}$	Critical and transition defect size estimation in Eq. (33)
$\sqrt{area_o}$	Murakami's initial defect size estimation in Eq. (25)
$\sqrt{area_R}$	Defect size estimation for surface roughness in Eq. (39) – Eq. (40)
Δa	Crack extension
$\alpha, \beta, \zeta, \delta$	Constants in Bi-parametric model Eq. (37)
$b(x, t)$	External body forces in Peridynamics Eq. (16)
C, m	Constants in Paris Eq. (3)
γ	Constant in Walker Eq. (11)
d_1	Length of microcrack threshold
d_2	Length of long crack threshold
D, p	Constants in Hartman-Schijve variant Eq. (14)
da/dN	Crack length per cycle
ε_{core}	Bond strain in Peridynamics Eq. (16)
f	Newman's crack closure factor Eq. (10)
H_x	All nearby points within a horizon in Peridynamics Eq. (16)
HV	Vicker's hardness
K_c	Fracture toughness
K_{min}	Minimum applied SIF
K_{max}	Maximum applied SIF
K_{op}	SIF when a crack first opens
$K_{max,o}, \Delta K_o, \alpha_o, \beta_o$	Constants in Doker's Stress Ratio Eq. (34) – Eq. (35)
ΔK	SIF range
ΔK_c	Overload SIF range
ΔK_{eff}	Effective SIF range
ΔK_{th}	Threshold SIF range (for long cracks)
$\Delta K_{th,SC}$	Threshold SIF range (for short cracks)
$\Delta K_{th,eff}$	Intrinsic threshold SIF range
$\Delta K_{th,op}$	Extrinsic threshold SIF range

ΔK_{thr}	Apparent threshold SIF range
$\Delta\kappa$	Schwalbe factor Eq. (13)
ℓ	Microstructural feature (μm)
λ, B	Constants in Peridynamics Eq. (16)
$p(x)$	Mass density of point x in Peridynamics Eq. (16)
R	Stress ratio
r, q	Constants in NASGRO Eq. (15)
σ_{min}	Minimum applied stress
σ_{max}	Maximum applied stress
$\Delta\sigma$	Stress range
$\Delta\sigma_e$	"Defect-free" fatigue strength
$\Delta\sigma_{th}$	Fatigue strength
t	Time in Peridynamics Eq. (16)
U	Elber's crack closure ratio Eq. (8)
$u(x,t)$	Displacement of material at point x and time t in Peridynamics Eq. (16)
$\ddot{u}(x,t)$	Acceleration of material at point x and time t in Peridynamics Eq. (16)
x	Position of a point in Peridynamics Eq. (16)
x'	Position of a neighboring point in Peridynamics Eq. (16)
Y	Geometry correction factor

References

1. Kundu, S.; Tech, B.; Tech, M. Durability and Damage Tolerance Assessment of Additively Manufactured (AM) Parts and AM Repairs.
2. Findlay, S.J.; Harrison, N.D. Why Aircraft Fail. *Mater. Today* **2002**, *5*, 18–25, doi:10.1016/S1369-7021(02)01138-0.
3. ASTM E647 Measurement of Fatigue Crack Growth Rates. **2015**, doi:10.1520/E0647-15E01.
4. Maierhofer, J.; Gänser, H.-P.; Pippan, R. Modified Kitagawa–Takahashi Diagram Accounting for Finite Notch Depths. *Int. J. Fatigue* **2015**, *70*, 503–509, doi:10.1016/j.ijfatigue.2014.07.007.
5. Jones, R.; Michopoulos, J.G.; Iliopoulos, A.P.; Singh Raman, R.K.; Phan, N.; Nguyen, T. Representing Crack Growth in Additively Manufactured Ti-6Al-4V. *Int. J. Fatigue* **2018**, *116*, 610–622, doi:10.1016/j.ijfatigue.2018.07.019.
6. Jones, R.; Singh Raman, R.K.; McMillan, A.J. Crack Growth: Does Microstructure Play a Role? *Eng. Fract. Mech.* **2018**, *187*, 190–210, doi:10.1016/j.engfracmech.2017.11.023.
7. Zerbst, U.; Vormwald, M.; Pippan, R.; Gänser, H.-P.; Sarrazin-Baudoux, C.; Madia, M. About the Fatigue Crack Propagation Threshold of Metals as a Design Criterion – A Review. *Eng. Fract. Mech.* **2016**, *153*, 190–243, doi:10.1016/j.engfracmech.2015.12.002.
8. Revankar, S.; Wolf, B.; Roznic, J. Metal Fatigue Crack Growth Models. *Int J Adv Eng App* **2012**, *5*, 85–91.
9. Zerbst, U.; Bruno, G.; Buffière, J.-Y.; Wegener, T.; Niendorf, T.; Wu, T.; Zhang, X.; Kashaev, N.; Meneghetti, G.; Hrabe, N.; et al. Damage Tolerant Design of Additively Manufactured Metallic Components Subjected to Cyclic Loading: State of the Art and Challenges. *Prog. Mater. Sci.* **2021**, *121*, 100786, doi:10.1016/j.pmatsci.2021.100786.
10. Galarraga, H.; Warren, R.J.; Lados, D.A.; Dehoff, R.R.; Kirka, M.M. Fatigue Crack Growth Mechanisms at the Microstructure Scale in As-Fabricated and Heat Treated Ti-6Al-4V ELI Manufactured by Electron Beam Melting (EBM). *Eng. Fract. Mech.* **2017**, *176*, 263–280, doi:10.1016/j.engfracmech.2017.03.024.
11. Oberwinkler, B. Modeling the Fatigue Crack Growth Behavior of Ti-6Al-4V by Considering Grain Size and Stress Ratio. *Mater. Sci. Eng. A* **2011**, *528*, 5983–5992, doi:10.1016/j.msea.2011.04.046.
12. Wycisk, E.; Solbach, A.; Siddique, S.; Herzog, D.; Walther, F.; Emmelmann, C. Effects of Defects in Laser Additive Manufactured Ti-6Al-4V on Fatigue Properties. *Phys. Procedia* **2014**, *56*, 371–378, doi:10.1016/j.phpro.2014.08.120.
13. Rigon, D.; Meneghetti, G. An Engineering Approach to Estimate Fatigue Thresholds of Wrought and Additively Manufactured Defective Metallic Materials. *Procedia Struct. Integr.* **2021**, *34*, 154–159, doi:10.1016/j.prostr.2021.12.022.

14. Iliopoulos, A.P.; Jones, R.; Michopoulos, J.G.; Phan, N.; Rans, C. Further Studies into Crack Growth in Additively Manufactured Materials. *Materials* **2020**, *13*, 2223, doi:10.3390/ma13102223.
15. Jones, R.; Rans, C.; Iliopoulos, A.P.; Michopoulos, J.G.; Phan, N.; Peng, D. Modelling the Variability and the Anisotropic Behaviour of Crack Growth in SLM Ti-6Al-4V. *Materials* **2021**, *14*, 1400, doi:10.3390/ma14061400.
16. Iliopoulos, A.; Jones, R.; Michopoulos, J.; Phan, N.; Singh Raman, R.K. Crack Growth in a Range of Additively Manufactured Aerospace Structural Materials. *Aerospace* **2018**, *5*, 118, doi:10.3390/aerospace5040118.
17. Madia, M.; Zerbst, U.; Werner, T. Estimation of the Kitagawa-Takahashi Diagram by Cyclic R Curve Analysis. *Procedia Struct. Integr.* **2022**, *38*, 309–316, doi:10.1016/j.prostr.2022.03.032.
18. Verma, R.; Kumar, P.; Jayaganthan, R.; Pathak, H. Extended Finite Element Simulation on Tensile, Fracture Toughness and Fatigue Crack Growth Behaviour of Additively Manufactured Ti6Al4V Alloy. *Theor. Appl. Fract. Mech.* **2022**, *117*, 103163, doi:10.1016/j.tafmec.2021.103163.
19. Liu, B.; Wang, K.; Bao, R.; Sui, F. The Effects of α / β Phase Interfaces on Fatigue Crack Deflections in Additively Manufactured Titanium Alloy: A Peridynamic Study. *Int. J. Fatigue* **2020**, *137*, 105622, doi:10.1016/j.ijfatigue.2020.105622.
20. Karpenko, O.; Oterkus, S.; Oterkus, E. Peridynamic Analysis to Investigate the Influence of Microstructure and Porosity on Fatigue Crack Propagation in Additively Manufactured Ti6Al4V. *Eng. Fract. Mech.* **2022**, *261*, 108212, doi:10.1016/j.engfracmech.2021.108212.
21. Masuo, H.; Tanaka, Y.; Morokoshi, S.; Yagura, H.; Uchida, T.; Yamamoto, Y.; Murakami, Y. Influence of Defects, Surface Roughness and HIP on the Fatigue Strength of Ti-6Al-4V Manufactured by Additive Manufacturing. *Int. J. Fatigue* **2018**, *117*, 163–179, doi:10.1016/j.ijfatigue.2018.07.020.
22. Nakatani, M.; Masuo, H.; Tanaka, Y.; Murakami, Y. Effect of Surface Roughness on Fatigue Strength of Ti-6Al-4V Alloy Manufactured by Additive Manufacturing. *Procedia Struct. Integr.* **2019**, *19*, 294–301, doi:10.1016/j.prostr.2019.12.032.
23. Rigon, D.; Meneghetti, G. An Engineering Estimation of Fatigue Thresholds from a Microstructural Size and Vickers Hardness: Application to Wrought and Additively Manufactured Metals. *Int. J. Fatigue* **2020**, *139*, 105796, doi:10.1016/j.ijfatigue.2020.105796.
24. Persenot, T.; Burr, A.; Martin, G.; Buffiere, J.-Y.; Dendievel, R.; Maire, E. Effect of Build Orientation on the Fatigue Properties of As-Built Electron Beam Melted Ti-6Al-4V Alloy. *Int. J. Fatigue* **2019**, *118*, 65–76, doi:10.1016/j.ijfatigue.2018.08.006.
25. Rigon, D.; Meneghetti, G. Estimating the Fatigue Thresholds of Additively Manufactured Metallic Materials with Consideration of Defects. *Procedia Struct. Integr.* **2022**, *38*, 70–76, doi:10.1016/j.prostr.2022.03.008.
26. Beretta, S.; Romano, S. A Comparison of Fatigue Strength Sensitivity to Defects for Materials Manufactured by AM or Traditional Processes. *Int. J. Fatigue* **2017**, *94*, 178–191, doi:10.1016/j.ijfatigue.2016.06.020.
27. Galati, M.; Iuliano, L. A Literature Review of Powder-Based Electron Beam Melting Focusing on Numerical Simulations. *Addit. Manuf.* **2018**, *19*, 1–20, doi:https://doi.org/10.1016/j.addma.2017.11.001.
28. Sames, W.J.; List, F.A.; Pannala, S.; Dehoff, R.R.; Babu, S.S. The Metallurgy and Processing Science of Metal Additive Manufacturing. *Int. Mater. Rev.* **2016**, *61*, 315–360, doi:10.1080/09506608.2015.1116649.
29. Paris, P.; Erdogan, F. A Critical Analysis of Crack Propagation Laws. *J. Basic Eng.* **1963**, *85*, 528–533.
30. Forman, R.G.; Kearney, V.E.; Engle, R.M. Numerical Analysis of Crack Propagation in Cyclic-Loaded Structures. *J. Basic Eng.* **1967**, *89*, 459–463, doi:10.1115/1.3609637.
31. Wolf, E. Fatigue Crack Closure under Cyclic Tension. *Eng. Fract. Mech.* **1970**, *2*, 37–45, doi:10.1016/0013-7944(70)90028-7.
32. Walker, K. The Effect of Load Ratio during Crack Propagation and Fatigue for 2024T3 and 7075-T6 Aluminum. *ASTM Selected Technical Papers* **1970**, *STP462*, 1–14, doi:10.1520/STP32032S.
33. Hartman, A.; Schijve, J. The Effects of Environment and Load Frequency on the Crack Propagation Law for Macro Fatigue Crack Growth in Aluminium Alloys. *Eng. Fract. Mech.* **1970**, *1*, 615–631, doi:10.1016/0013-7944(70)90003-2.

34. Klesnil, M.; Lukáš, P. Influence of Strength and Stress History on Growth and Stabilisation of Fatigue Cracks. *Eng. Fract. Mech.* **1972**, *4*, 77–92, doi:10.1016/0013-7944(72)90078-1.
35. Jones, R. Fatigue Crack Growth and Damage Tolerance. *Fatigue Fract. Eng. Mater. Struct.* **2014**, *37*, 463–483, doi:10.1111/ffe.12155.
36. Tanaka, K.; Akiniwa, Y. Resistance-Curve Method for Predicting Propagation Threshold of Short Fatigue Cracks at Notches. *Eng. Fract. Mech.* **1988**, *30*, 863–876, doi:https://doi.org/10.1016/0013-7944(88)90146-4.
37. Doker, H. Fatigue Crack Growth Threshold: Implications, Determination and Data Evaluation. *Int J Fatigue* **1997**, *19*, 145–149, doi:10.1016/S0142-1123(97)00058-3.
38. Newman Jr., J.C. FASTRAN-2: A Fatigue Crack Growth Structural Analysis Program. *NASA TM-104159* **1992**.
39. Schwalbe, K.-H. On the Beauty of Analytical Models for Fatigue Crack Propagation and Fracture – A Personal Historical Review. *J. ASTM Int.* **2010**, *7*.
40. Moes, N.; Dolbow, J.; Belytschko, T. A Finite Element Method for Crack Growth without Remeshing. *Int. J. Numer. Meth. Engng.* **1999**, *46*, 131–150, doi:10.1002/(SICI)1097-0207(19990910)46.
41. Silling, S.A. Reformulation of Elasticity Theory for Discontinuities and Long-Range Forces.
42. Silling, S.A.; Lehoucq, R.B. Peridynamic Theory of Solid Mechanics. *Advances in Applied Mechanics* **2010**, *44*, 73–168, doi:10.1016/S0065-2156(10)44002-8.
43. Silling, S.; Askari, A. *Peridynamic Model for Fatigue Cracking.*; 2014; pp. SAND2014-18590, 1160289, 540395;.
44. Haddad, M.H.E.; Topper, T.H.; Smith, K.N. Prediction of Non Propagating Cracks. *Eng. Fract. Mech.* **1979**, *11*, 573–584, doi:https://doi.org/10.1016/0013-7944(79)90081-X.
45. Murakami, Y. *Metal Fatigue: Effects of Small Defects and Nonmetallic Inclusions*; Referex Engineering; Elsevier, 2002; ISBN 978-0-08-044064-4.
46. Kitagawa, H. Applicability of Fracture Mechanics to Very Small Cracks or the Cracks in the Early Stage. *Proc. of 2nd ICM, Cleveland* **1976**, 627–631.
47. Zerbst, U.; Vormwald, M.; Pippan, R.; Gänser, H.-P.; Sarrazin-Baudoux, C.; Madia, M. About the Fatigue Crack Propagation Threshold of Metals as a Design Criterion – A Review. *Eng. Fract. Mech.* **2016**, *153*, 190–243, doi:10.1016/j.engfracmech.2015.12.002.
48. Akiniwa, Y.; Zhang, L.M.; Tanaka, K. PREDICTION OF THE FATIGUE LIMIT OF CRACKED SPECIMENS BASED ON THE CYCLIC *R* -CURVE METHOD. *Fatigue Fract. Eng. Mater. Struct.* **1997**, *20*, 1387–1398, doi:10.1111/j.1460-2695.1997.tb01497.x.
49. Murakami, Y.; Masahiro, E. Quantitative Evaluation of Fatigue Strength of Metals Containing Various Small Defects or Cracks. *Eng. Fract. Mech.* **1983**, *17*, 1–15, doi:10.1016/0013-7944(83)90018-8.
50. Yoder, G.R.; Cooley, L.A.; Crooker, T.W. On Microstructural Control of Near-Threshold Fatigue Crack Growth in 7000-Series Aluminum Alloys. *Scr. Metall.* **1982**, *16*, 1021–1025, doi:10.1016/0036-9748(82)90448-3.
51. Herold, H.; Streitenberger, M.; Zinke, M.; Orazi, L.; Cammarota, G.P. An Experimental and Theoretical Approach for an Estimation of ΔK_{th}. *Fatigue Fract. Eng. Mater. Struct.* **2000**, *23*, 805–812, doi:10.1046/j.1460-2695.2000.00314.x.
52. Jones, R.; Kovarik, O.; Cizek, J.; Ang, A.; Lang, J. Crack Growth in Conventionally Manufactured Pure Nickel, Titanium and Aluminum and the Cold Spray Addively Manufactured Equivalents. *Additive Manufacturing Letters* **2022**, *3*, doi:10.1016/j.addlet.2022.100043.
53. Jones, R.; Cizek, J.; Kovarik, O.; Lang, J.; Ang, A.; Michopoulos, J.G. Describing Crack Growth in Additively Manufactured Scalmalloy. *Additive Manufacturing Letters* **2021**, *1*, doi:10.1016/j.addlet.2021.100020.
54. Seifi, M.; Salem, A.; Satko, D.; Shaffer, J.; Lewandowski, J.J. Defect Distribution and Microstructure Heterogeneity Effects on Fracture Resistance and Fatigue Behavior of EBM Ti–6Al–4V. *Int. J. Fatigue* **2017**, *94*, 263–287, doi:10.1016/j.ijfatigue.2016.06.001.
55. Draper, S.; Lerch, B.; Rogers, R.; Martin, R.; Locci, I.; Garg, A. Materials Characterization of Electron Beam Melted Ti-6Al-4V. In *Proceedings of the 13th World Conference on Titanium*; Venkatesh, V., Pilchak, A.L., Allison, J.E., Ankem, S., Boyer, R., Christodoulou, J., Fraser, H.L., Imam, M.A., Kosaka, Y., Rack, H.J., Chatterjee, A., Woodfield, A., Eds.; Wiley, 2016; pp. 1433–1440 ISBN 978-1-119-28326-3.

56. Zhai, Y.; Galarraga, H.; Lados, D.A. Microstructure, Static Properties, and Fatigue Crack Growth Mechanisms in Ti-6Al-4V Fabricated by Additive Manufacturing: LENS and EBM. *Eng. Fail. Anal.* **2016**, *69*, 3–14, doi:10.1016/j.engfailanal.2016.05.036.
57. Greitemeier, D.; Palm, F.; Syassen, F.; Melz, T. Fatigue Performance of Additive Manufactured TiAl6V4 Using Electron and Laser Beam Melting. *Int. J. Fatigue* **2017**, *94*, 211–217, doi:10.1016/j.ijfatigue.2016.05.001.
58. Edwards, P.; O'Conner, A.; M, R. Electron Beam Additive Manufacturing of Titanium Components: Properties and Performance. *J. Manuf. Sci. Eng.* **2013**, *135*, 061016, doi:10.1115/1.4025773.
59. Kirchner, A.; Klöden, B.; Weißgärber, T.; Kieback, B.; Schoberth, A.; Bagehorn, S.; Greitemeier, D. Mechanical Properties of Ti-6Al-4V Additively Manufactured by Electron Beam Melting.
60. Zhang, H.; Yao, L.; Zheng, X.; Zhou, J. A Whole-Rate-Region Fatigue Crack Growth Model Incorporating Nonlinear Rate Evolution Characteristics Based on a Peridynamic Approach. *J. Eng. Mech.* **2024**, *150*, 04024094, doi:10.1061/JENMDT.EMENG-7962.
61. Chi, W.; Wang, W.; Zhou, H.; Yan, R.; Mikami, Y. Multiscale Modelling of Additively Manufactured Ti-6Al-4V Alloy: Fatigue Performance Evaluation from Material to Structural Level. *Int. J. Fatigue* **2025**, *201*, 109181, doi:10.1016/j.ijfatigue.2025.109181.
62. Bergant, M.A.; Soria, S.R.; Bustos, R.I.; Soul, H.R.; Yawny, A.A. On the Relative Significance of Roughness, Printing Defects and Microstructure on the Fatigue Behavior of Electron Beam Melted Ti-6Al-4V. *Fatigue Fract. Eng. Mater. Struct.* **2025**, *48*, 1647–1666, doi:10.1111/ffe.14565.
63. Chandran, K.S.R. The Finding of the Reciprocal Relationship between Fatigue (S-N) Behavior and Fatigue Crack Growth Behavior Enabling Interconversion of Data in Structural Materials. *Materialia* **2022**, *25*, 101541, doi:10.1016/j.mtla.2022.101541.
64. Macallister, N.; Becker, T.H. Fatigue Life Estimation of Additively Manufactured Ti-6Al-4V: Sensitivity, Scatter and Defect Description in Damage-Tolerant Models. *Acta Mater.* **2022**, *237*, 118189, doi:10.1016/j.actamat.2022.118189.
65. Chapetti, M.D. Fracture Mechanics for Fatigue Design of Metallic Components and Small Defect Assessment. *International Journal of Fatigue* **2022**, *154*, 106550, doi:10.1016/j.ijfatigue.2021.106550.
66. Duarte, L.; Schönherr, J.A.; Madia, M.; Zerbst, U.; Geilen, M.B.; Klein, M.; Oechsner, M. Recent Developments in the Determination of Fatigue Crack Propagation Thresholds. *International Journal of Fatigue* **2022**, *164*, 107131, doi:10.1016/j.ijfatigue.2022.107131.
67. Martins, R.F.; Branco, R.; Camacho, J.; Macek, W.; Marciniak, Z.; Silva, A.; Malça, C. The Influence of Printing Strategies on the Fatigue Crack Growth Behaviour of an Additively Manufactured Ti6Al4V Grade 23 Titanium Alloy. *International Journal of Fatigue* **2025**, *197*, 108942, doi:10.1016/j.ijfatigue.2025.108942.
68. Yi, M.; Tang, W.; Zhu, Y.; Liang, C.; Tang, Z.; Yin, Y.; He, W.; Sun, S.; Su, S. A Holistic Review on Fatigue Properties of Additively Manufactured Metals. *Journal of Materials Processing Technology* **2024**, *329*, 118425, doi:10.1016/j.jmatprotec.2024.118425.